

## Supporting information

# Voltammetric and Amperometric Determination of Iodate using Ionic Liquid/Polyoxotungstate/MWCNTs-COOH Organic-Inorganic Nanohybrid Modified Glassy Carbon Electrode

Atefeh Karimi-Takallo, Somayeh Dianat\*

Department of Chemistry, Faculty of Sciences, University of Hormozgan, Bandar Abbas 79161-93145, Iran

---

### *Characterization*

The carbon, nitrogen, potassium, phosphorus, tungsten, and cobalt content of (bdpy)PW<sub>11</sub>Co were analyzed by elemental analysis. Theoretical value [%]: C: 9.72; N: 1.62; K: 1.13; P: 0.90; W: 56.52; Co: 1.70. Experimental value [%]: C: 9.73; N: 1.60; K: 1.14; P: 0.89; W: 56.55; Co: 1.68.

These results confirm the molar ratios of W:P:Co = 10.8:1.0:1.0 demonstrating that the Keggin structure of PW<sub>11</sub>Co has maintained during the functionalization with bdpy ionic liquid. The loading percentage of (bdpy)PW<sub>11</sub>Co on the MWCNTs-COOH matrix was estimated 0.36 % by ICP spectroscopy.

Fig. 1S-A, curve e shows the ATR-FTIR spectrum of (bdpy)PW<sub>11</sub>Co/MWCNTs-COOH. The peaks nearby 1744, 1178 cm<sup>-1</sup> belong to the stretching vibration of COOH of MWCNTs and C-N of bdpy, respectively. The peaks around 1603, 1435 cm<sup>-1</sup> belong to the stretching vibration of C=C aromatic of the MWCNTs-COOH and bdpy. Also, the four characteristic absorption peaks can be observed in the range of 1100 to 800 cm<sup>-1</sup>, belonging to  $\nu_{as}$  (P-O<sub>a</sub>),  $\nu_{as}$  (W-O<sub>d</sub>),  $\nu_{as}$  (W-O<sub>b</sub>-W), and  $\nu_{as}$  (W-O<sub>c</sub>-W), respectively. The existence of these asymmetric stretching vibration peaks suggests that the POM moiety of this hybrid compound has still kept its Keggin structure. In order to have a better comparison, ATR-FTIR spectra of PW<sub>11</sub>Co, (bdpy)PW<sub>11</sub>Co, bdpy, and MWCNTs-COOH were also recorded as displayed in Fig. 1S-A curves a, b, c, d, respectively.

---

Corresponding author:

\*Tel.: +98 76 33670121, Email Address: [s.dianat@hormozgan.ac.ir](mailto:s.dianat@hormozgan.ac.ir)

The UV-vis spectrum of  $PW_{11}Co$  (Fig. 1S-B, curve a) shows bands associated with terminal  $W-O_d$  ( $O_d$ , terminal oxygen) links for  $O_d \rightarrow W$  charge transfer, and  $W-O_{b/c}-W$  ( $O_b$ ,  $O_c$ , bridging oxygen) characteristic tri-centric links that attributed to  $O_b/O_c \rightarrow W$  charge transfer transitions. According to previous literature data,  $O_d \rightarrow W$  charge transfer transition occurs at 185–195 nm with high molar absorption coefficient [69-71]. Therefore, only the peak tail corresponding to  $W-O_d$  appears in the spectrum (absorptions at about 200 nm), but we noticed that the peak was very strong, which corresponds to higher binding energies. The second peak at 250 nm is characteristic for  $W-O_{b/c}-W$  bounds. Moreover, a broad and weak peak in the visible region at 538 nm appeared in the spectrum (inset of Fig. 1S-B). This pattern is typical for octahedral cobalt (II) complexes and can be assigned to  ${}^4T_{1g}(F) \rightarrow {}^4T_{1g}(P)$  transition [72].

UV-vis spectrum of  $bdpy$  (Fig. 1S-B, curve b) shows an absorption peak and an absorption shoulder at 258 and 265nm, respectively. Since pyridine is existent in the structure of  $bdpy$  ionic liquid and on the other hand, pyridine is a heterocyclic compound, so these peaks show the electronic transitions resulting from the  $\pi \rightarrow \pi^*$  and  $n \rightarrow \pi^*$  transitions. For  $(bdpy)PW_{11}Co$  hybrid compound, in addition to these absorption bands, an absorption band at 288 nm also appeared that is ascribed to  $O_b/O_c \rightarrow W$  transitions with red-shift (Fig. 1S-B, curve c). The red-shift of the  $O_b/O_c \rightarrow W$  transitions is correlated to the interactions between the polyoxoanion and organic cation.

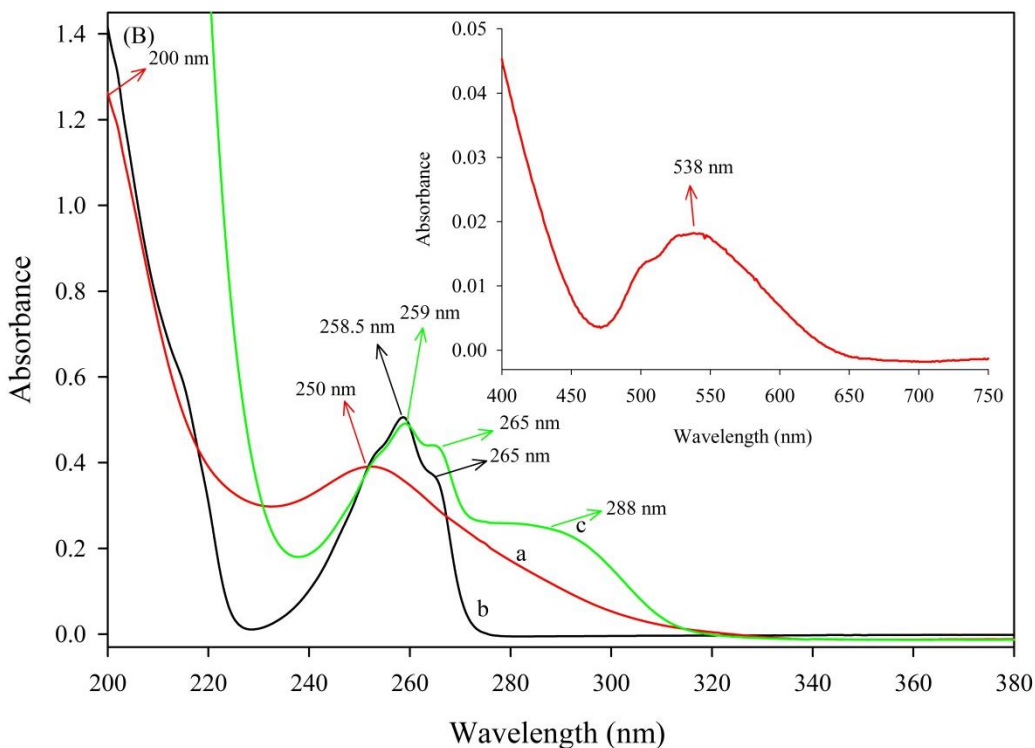
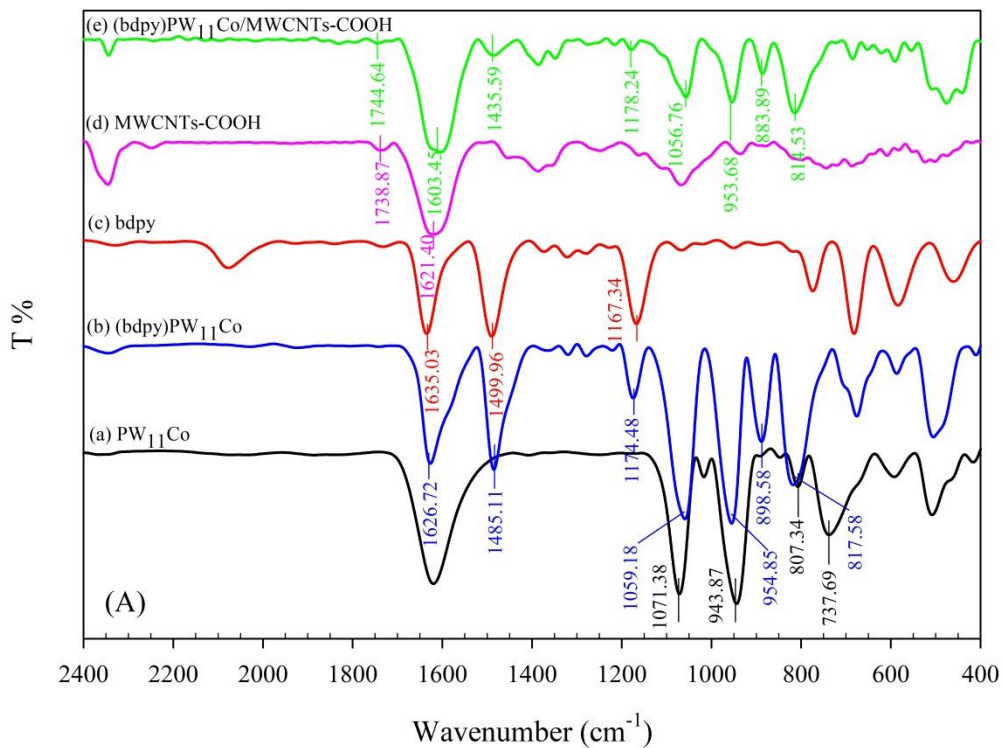


**Fig. 1S** (A) ATR-FTIR spectra of PW<sub>11</sub>Co (a), (bdpy)PW<sub>11</sub>Co (b), bdpy (c), MWCNTs-COOH (d), and (bdpy)PW<sub>11</sub>Co/MWCNTs-COOH (e), (B) UV-Vis spectra of PW<sub>11</sub>Co (a), bdpy (b) in deionized water, and (bdpy)PW<sub>11</sub>Co (c) in acetonitrile.

X-ray diffraction (XRD) study is performed for characterization of the crystalline structure of the (bdpy)PW<sub>11</sub>Co/MWCNTs-COOH. The XRD patterns of PW<sub>11</sub>Co, bdpy, (bdpy)PW<sub>11</sub>Co, MWCNTs-COOH, and (bdpy)PW<sub>11</sub>Co/MWCNTs-COOH are presented in Fig. 2S. As shown in Fig. 2S-b, (bdpy)PW<sub>11</sub>Co displays (110), (011), (220), (123), and (033) diffraction peaks, located at 8.2°, 9.5°, 16.5°, 28.6°, and 30.6°, respectively of the PW<sub>11</sub>Co (Fig. 2S-a). Other obvious characteristic peaks, at 15.8°, 20.7°, 22.3°, and 24.3°, can be attributed to the organic part (Fig. 2S-c).

Fig. 2S-d shows two characteristic peaks at 26° and 43°, which are corresponding to (002) and (100) reflections of graphite from the MWCNTs-COOH, respectively. These results are consistent with the previous literature [73, 74]. In Fig. 2S-e, the characteristic XRD peaks of (bdpy)PW<sub>11</sub>Co/MWCNTs-COOH appeared at nearly the similar locations without significant shift in its peaks position compared to those of PW<sub>11</sub>Co. It indicates that PW<sub>11</sub>Co specie in the (bdpy)PW<sub>11</sub>Co/MWCNTs-COOH hybrid nanocomposite still keeps the Keggin structure. Furthermore, the presence of the characteristic peaks at 26° (002), confirmed that (bdpy)PW<sub>11</sub>Co was immobilized on the MWCNTs-COOH surface.

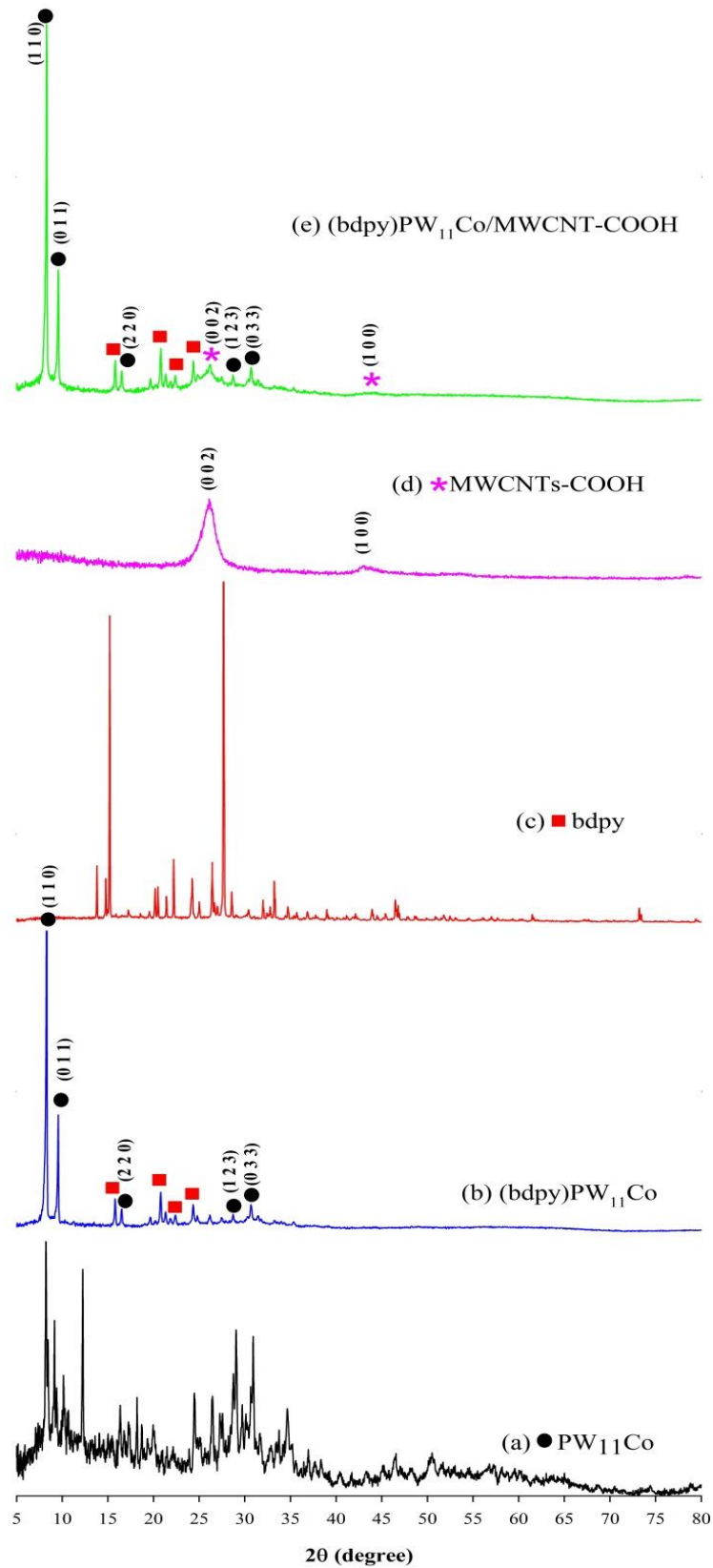


**Fig. 2S** XRD patterns of PW<sub>11</sub>Co (a), (bdpy)PW<sub>11</sub>Co (b), bdpy (c), MWCNTs-COOH (d), and (bdpy)PW<sub>11</sub>Co/MWCNTs-COOH (e).

The thermogravimetric/differential thermal analysis (TGA/DTA) curves for bdp<sub>y</sub>, PW<sub>11</sub>Co, and (bdp<sub>y</sub>)PW<sub>11</sub>Co hybrid material under the air atmosphere are presented in Fig. 3S. The TGA curve of bdp<sub>y</sub> shows a major weight loss (about 61.3%) at 250-320°C, (Fig. 3S-a), as indicated in the 3<sup>rd</sup> peak of the DTA curve. It can be attributed to the decomposition of pyridine rings in the structure of bdp<sub>y</sub>. The thermal response of PW<sub>11</sub>Co (Fig. 3S-b) showed a minor weight loss (about 8%) at 25–200°C across two steps (1<sup>st</sup> and 2<sup>nd</sup> peaks of DTA) which demonstrates the high thermal stability of PW<sub>11</sub>Co up to 800°C. These small changes in the mass would be related to the elimination of water of crystallization from the crystal lattice of PW<sub>11</sub>Co. The thermal stability of the hybrid material is completely enhanced compared to the parent bdp<sub>y</sub> but is less than the original polyoxoanion (Fig. 3S-c). Below 350°C, no major loss in weight can be seen which demonstrates the water content in the hybrid material was reduced but not quite lost because several small exothermic peaks can be observed in this range of temperatures. Above 350°C, major weight loss is observed, which is valued 13.4% at 300-450°C and 52.7% at 550-700°C. After these stages, the residual mass of about 34% remains constant from 700 to 800°C without any further decomposition. However, the first loss step in the weight would be correlated to the oxidative decomposition of IL part of (bdp<sub>y</sub>)PW<sub>11</sub>Co/MWCNTs-COOH. The second change step can be attributed to the degradation of MWCNTs-COOH support in the structure of this organic-inorganic hybrid composite.

The morphology, and microstructure of the (bdp<sub>y</sub>)PW<sub>11</sub>Co/MWCNTs-COOH was compared with the MWCNTs-COOH at different magnifications by transmission electron microscopy (TEM), as depicted in Fig. 4S. TEM images of (bdp<sub>y</sub>)PW<sub>11</sub>Co/MWCNTs-COOH demonstrate that (bdp<sub>y</sub>)PW<sub>11</sub>Co nanoparticles were distributed homogeneously on the surfaces or their interlayers of MWCNTs-COOH with an average diameter of 8.5 nm. Such homogeneous distribution of the (bdp<sub>y</sub>)PW<sub>11</sub>Co nanoparticles in an interlaced structure increased the electrochemical activity.

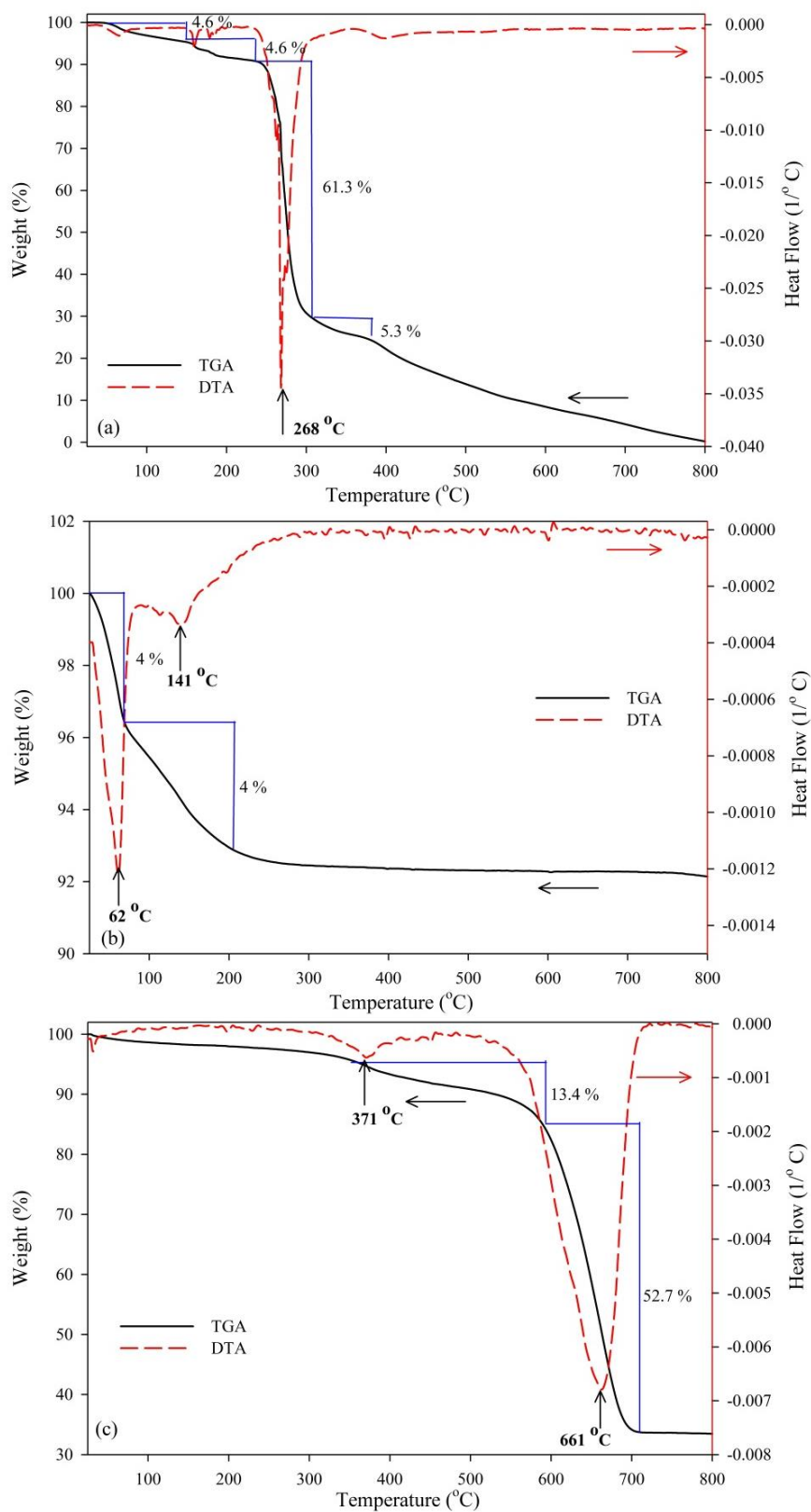


**Fig. 3S** TGA-DTA curves of bdpY (a), PW<sub>11</sub>Co (b), and (bdpY)PW<sub>11</sub>Co/MWCNTs-COOH (c) in the temperature range of 25-800°C at a heating rate of 10°C min<sup>-1</sup>.

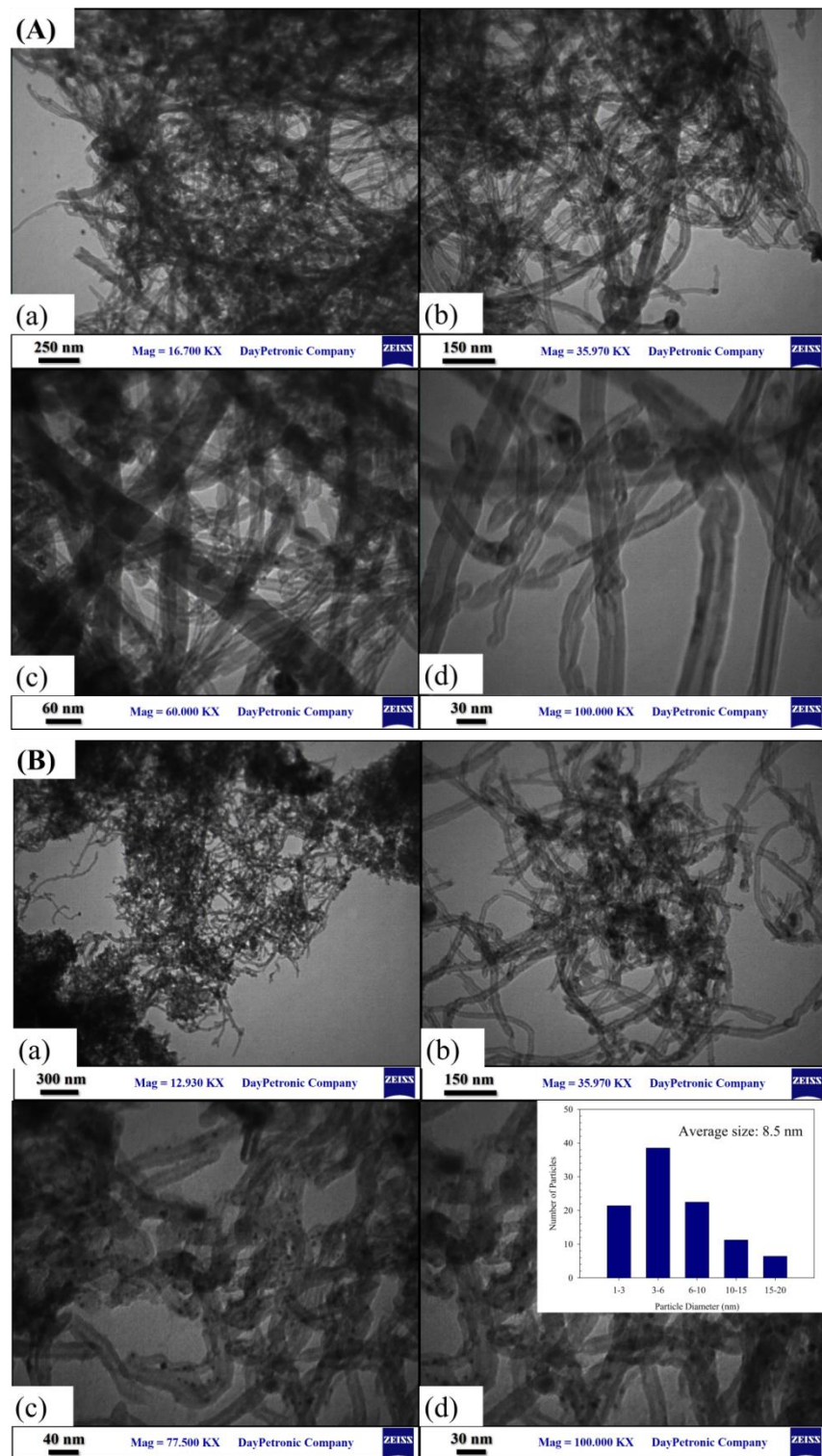


**Fig. 4S** TEM images of (A) MWCNTs-COOH (a, b, c, d) and (B) (bdpy)PW<sub>11</sub>Co/MWCNTs-COOH (a, b, c, d) at different magnifications. The inset of image (d) shows size distribution histogram of (bdpy)PW<sub>11</sub>Co/MWCNTs-COOH.

Fig. 5S-A shows the Cyclic voltammograms (CVs) of the bare GCE,  $\text{PW}_{11}\text{Co}/\text{GCE}$ ,  $\text{bdpy}/\text{GCE}$ ,  $(\text{bdpy})\text{PW}_{11}\text{Co}/\text{GCE}$ , and  $(\text{bdpy})\text{PW}_{11}\text{Co}/\text{MWCNTs-COOH}/\text{GCE}$  in  $0.1 \text{ mol L}^{-1} \text{ HClO}_4$  aqueous solution (pH 1.5). There is no clear redox peak for the bare GCE,  $\text{PW}_{11}\text{Co}/\text{GCE}$ ,  $\text{bdpy}/\text{GCE}$  and  $(\text{bdpy})\text{PW}_{11}\text{Co}/\text{GCE}$  in the studied potential range (Fig. 5S-A, curves a, b, c, d, respectively). ILs are electroactive in non-aqueous electrolytes [75]. For this reason, no specific peak of these compounds was observed in aqueous conditions. But, the background current of  $(\text{bdpy})\text{PW}_{11}\text{Co}/\text{GCE}$  (curve d) is less than the background current of  $\text{PW}_{11}\text{Co}/\text{GCE}$  (curve b), which is due to the high ionic conductivity of  $\text{bdpy}$ . However, at the  $(\text{bdpy})\text{PW}_{11}\text{Co}/\text{MWCNTs-COOH}/\text{GCE}$  (Fig. 5S-A, curve e), two pairs of pseudo-reversible redox peaks with the half wave potentials ( $E_{1/2} = (E_{p,a} + E_{p,c})/2$ ), of  $-0.404 \text{ (I,I')} \text{ and } -0.624 \text{ (II,II')} \text{ V vs. Ag/AgCl}$ , can be obviously observed, resulting from the two sequential one-electron processes relating to  $\text{W}^{\text{VI}} \rightarrow \text{W}^{\text{V}} \rightarrow \text{W}^{\text{IV}}$ . This phenomenon means that  $\text{MWCNTs-COOH}$  support can facilitate the electron transfer between the GCE and  $(\text{bdpy})\text{PW}_{11}\text{Co}$  in a most effective path (compare curve d with e).

Fig. 5S-B shows the CVs of the  $(\text{bdpy})\text{PW}_{11}\text{Co}/\text{MWCNTs-COOH}/\text{GCE}$  in  $\text{HClO}_4$  ( $0.1 \text{ mol L}^{-1}$ , pH 1.5) at different scan rates ( $10$  to  $300 \text{ mVs}^{-1}$ ). As can be seen, with increasing scan rate, the cathodic/anodic ( $\text{I/I}'$ ) peak currents increase linearly in the range from  $10$  to  $300 \text{ mV s}^{-1}$  (inset of Fig. 5S-B), indicating that electrochemical behavior of POM immobilized on the GCE is surface-controlled. Moreover, the peaks potential did not change meaningfully with increasing scan rate, suggesting that the electron transfer kinetics were very fast on the modified electrode surface.

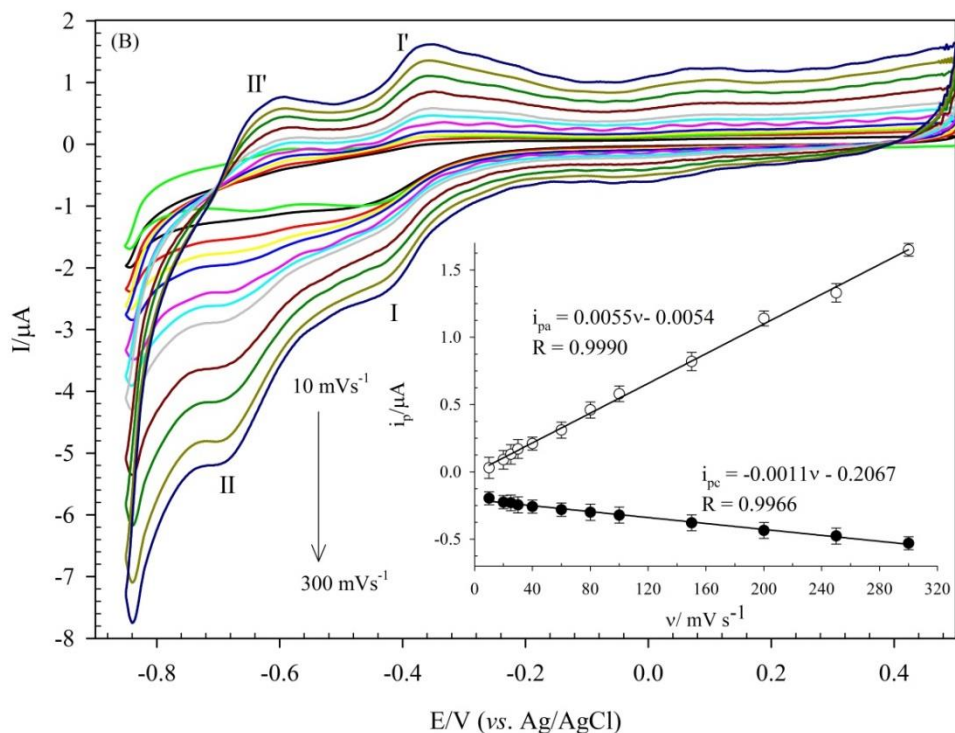
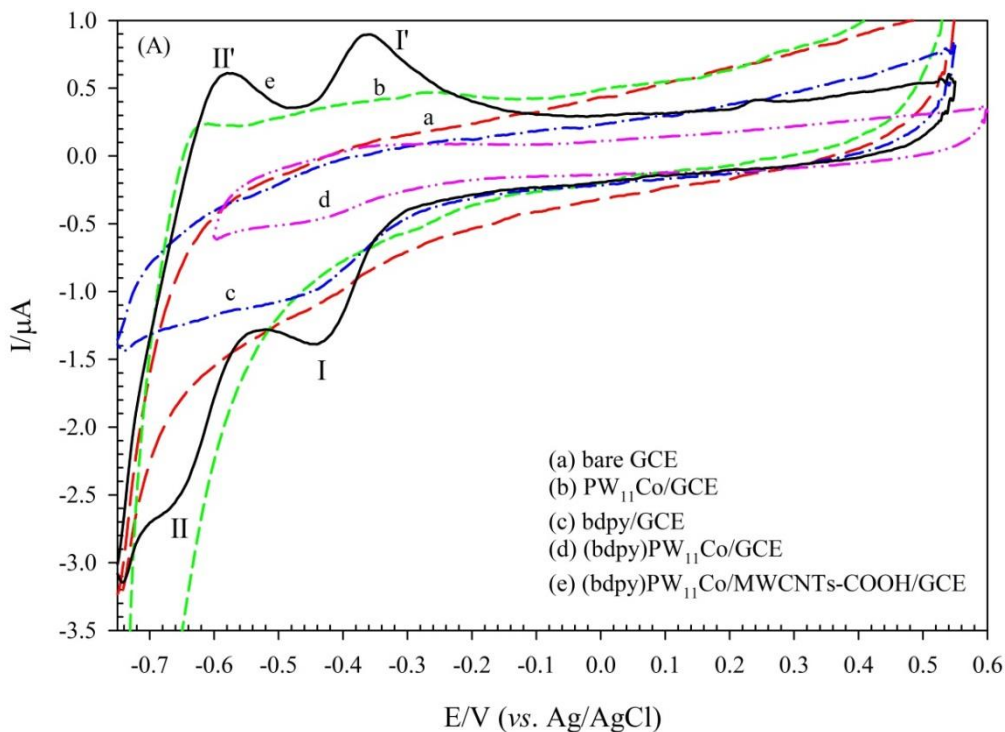


**Fig. 5S** (A) Cyclic voltammograms obtained on the bare GCE (a),  $PW_{11}Co/GCE$  (b), bdp/GCE (c), (bdpy) $PW_{11}Co/GCE$  (d), and (bdpy) $PW_{11}Co/MWCNTs-COOH/GCE$  (e) in  $HClO_4$  ( $0.1\text{ mol L}^{-1}$ , pH 1.5) and scan rate of  $100\text{ mVs}^{-1}$  and (B) Cyclic voltammogram of the (bdpy) $PW_{11}Co/MWCNTs-COOH/GCE$  in  $HClO_4$  ( $0.1\text{ mol L}^{-1}$ , pH 1.5) at different scan rates from 10 to  $300\text{ mVs}^{-1}$ . The inset shows variations of the cathodic (●) and anodic (○) peak currents with scan rates for I/I' peak

$K_3[Fe(CN)_6]$  ( $0.5 \text{ mmol L}^{-1}$ ) was chosen as a redox probe to evaluate the interfacial electron transfer properties of the bare and modified GCEs. As shown in Fig. 6S-A, the electrochemical peaks current of the GCE before and after modification were changed. The electron transfer kinetics of the  $Fe(CN)_6^{3-/4-}$  redox pair at the interface of the modified GCEs depends on the thickness and electronic structure of the modifier. According to Fig. 6S-A, curve a, it appears a pair of well-defined redox peaks at the bare GCE with a  $\Delta E_p$  around 93 mV in  $Fe(CN)_6^{3-/4-}$  solution, at pH 3. The presence of the  $PW_{11}Co$  on the GCE acts as a barrier layer and due to electrostatic repulsion, decreased the faradaic peak currents ( $i_p$ ) and increased  $\Delta E_p$  (Fig. 6S-A, compare curves a, and d). These findings are in agreement with previous studies [27].

However, a better reversible behavior (smaller  $\Delta E_p$ ) accompanied by an increase of  $i_p$ , is observed for the MWCNTs-COOH/GCE, bdpY/GCE, and (bdpy) $PW_{11}Co$ /MWCNTs-COOH/GCE compared with bare GCE (Fig. 6S-A, curve b, c, and e). The better electrochemical activity of these modified GCEs can be attributed to the excellent conductivity of the MWCNTs-COOH, bdpY ionic liquid, and (bdpy) $PW_{11}Co$ /MWCNTs-COOH on the surface of the bare GCE. The obtained quantitative information from CV on the bare and modified GCEs in the presence of  $0.5 \text{ mmol L}^{-1} [Fe(CN)_6]^{3-/4-}$  in PBS ( $10.0 \text{ mmol L}^{-1}$ , pH 3) containing  $0.1 \text{ mol L}^{-1}$  KCl as a supporting electrolyte is illustrated in Table 1S.

Fig. 6S-B shows the CVs of (bdpy) $PW_{11}Co$ /MWCNTs-COOH/GCE in the presence of  $0.5 \text{ mmol L}^{-1} [Fe(CN)_6]^{3-/4-}$  solution in  $10.0 \text{ mmol L}^{-1}$  PBS containing  $0.1 \text{ mol L}^{-1}$  KCl at the different pHs (pH 3-9). As shown in Fig. 6S-B, with pH increasing, the  $i_p$  decrease and the  $\Delta E_p$  increases. This behavior can be explained as follows: pH-metric titration plots obtained using a variation of the  $\Delta E_p$  and  $i_p$  of (bdpy) $PW_{11}Co$ /MWCNTs-COOH/GCE versus pH gave a surface  $pK_a$  of 5.1, and thus, a positive charge-state of the surface at lower pH values (inset of Fig. 6S-B). Therefore, it can be supposed that the decreases in  $\Delta E_p$ , as well as the increases in  $i_p$  of the modified surface at acidic solutions, have been affected by electrostatic interaction between the positively charged the surface of (bdpy) $PW_{11}Co$ /MWCNTs-COOH/GCE and  $[Fe(CN)_6]^{3-/4-}$  redox probe.

The electroactive surface area of the modified electrode was estimated by performing CV measurement at the (bdpy) $PW_{11}Co$ /MWCNTs-COOH/GCE in  $0.5 \text{ mmol L}^{-1} [Fe(CN)_6]^{3-/4-}$  solution in  $10.0 \text{ mmol L}^{-1}$  PBS,

pH 3 containing 0.1 mol L<sup>-1</sup> KCl at different scan rates in the range of 10-140 mVs<sup>-1</sup> (Fig. 6S-C).

According to the Randles-Sevcik equation [76, 77], the surface area was calculated by Eq. 1S.

$$i_p = 2.69 \times 10^5 n^{3/2} A_{eff} D_0^{1/2} \nu^{1/2} C_p \quad (1S)$$

Where,  $i_p$  is the peak current (A),  $n$  is the number of transferred electrons,  $A_{eff}$  is the effective surface area (cm<sup>2</sup>),  $D_0$  is the diffusion coefficient of [Fe(CN)<sub>6</sub>]<sup>3-/4-</sup> (7.6×10<sup>-6</sup> cm<sup>2</sup>s<sup>-1</sup>),  $\nu^{1/2}$  is the square root of scan rate (Vs<sup>-1</sup>)<sup>1/2</sup>, and  $C_p$  is the concentration of the probe solution (mol L<sup>-1</sup>). The effective surface area of the (bdpy)PW<sub>11</sub>Co/MWCNTs-COOH/GCE is calculated to be 0.989 cm<sup>2</sup> according to the calibration equation of  $i_p = -0.3658\nu^{1/2} + 0.2808$  (R<sup>2</sup>= 0.9965) shown in inset of Fig. 6S-C, which is nearly 31 times larger than the bare electrode (0.0314 cm<sup>2</sup>). However, the high electroactive surface area of the (bdpy)PW<sub>11</sub>Co/MWCNTs-COOH/GCE led to enhancing the electrocatalytic activity, which is confirmed in the following part.

**Table 1S.** Electrochemical parameters extracted from CVs (Fig. 6S-A) on the bare and modified GCEs in the presence of [Fe(CN)<sub>6</sub>]<sup>3-/4-</sup> (0.5 mmol L<sup>-1</sup>) in PBS (10.0 mmol L<sup>-1</sup>, pH 3) containing KCl (0.1 mol L<sup>-1</sup>) as supporting electrolyte.

Electrode	$i_{pa}$ (μA) ± SD <sup>a</sup>	$i_{pc}$ (μA) ± SD <sup>a</sup>	$\Delta E_p$ (mV) ± SD <sup>a</sup>
Bare GCE	1.54 ± 0.10	1.72 ± 0.13	92.6 ± 5
MWCNTs-COOH/GCE	1.39 ± 0.08	2.21 ± 0.08	80.6 ± 6
bdpy/GCE	1.66 ± 0.07	1.96 ± 0.10	85.3 ± 8
PW <sub>11</sub> Co/GCE	1.28 ± 0.11	1.44 ± 0.12	122.4 ± 4
(bdpy)PW <sub>11</sub> Co/MWCNTs-COOH/GCE	1.85 ± 0.09	2.42 ± 0.15	73.3 ± 4

<sup>a</sup> SD: Standard Deviation (from 3 data point)

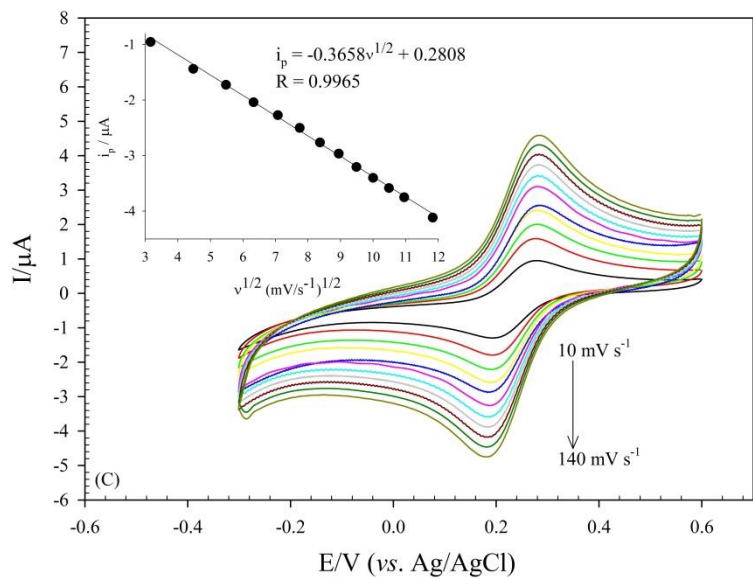
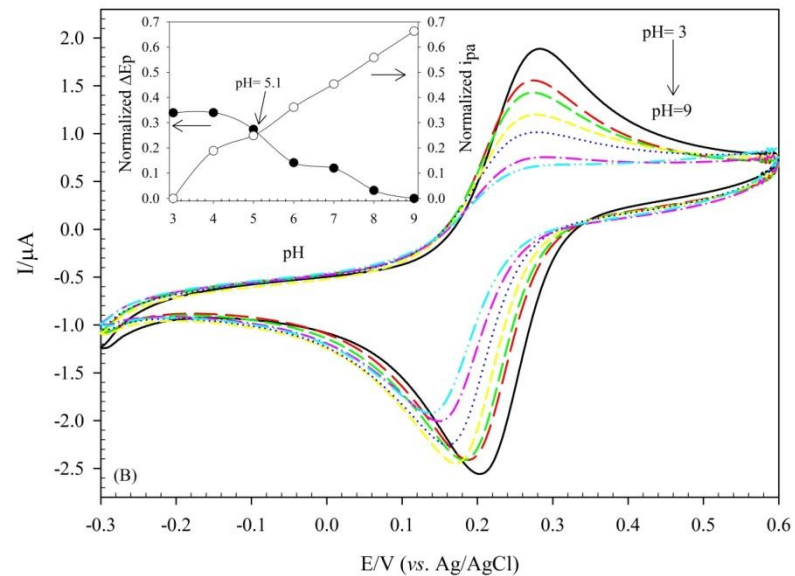
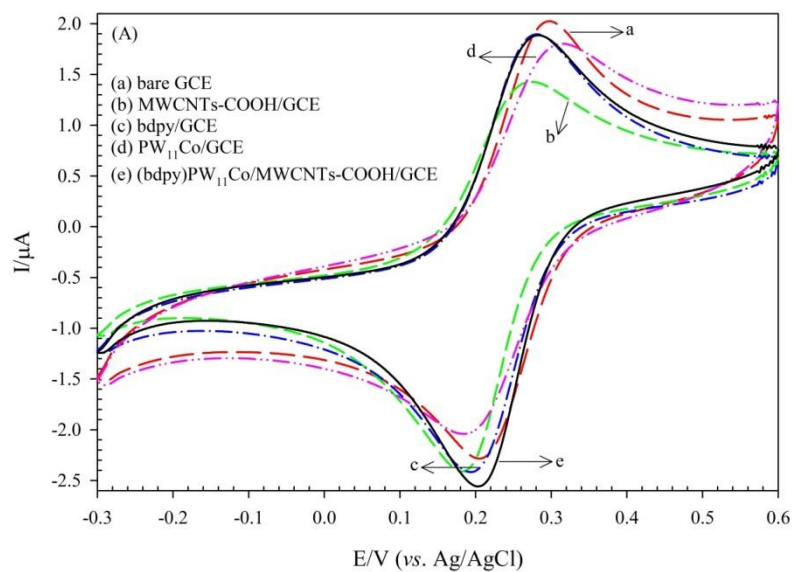


**Fig. 6S** Cyclic voltammograms obtained in the presence of  $0.5 \text{ mmol L}^{-1}$   $[\text{Fe}(\text{CN})_6]^{3-/4-}$  as a redox probe, in PBS solution ( $10.0 \text{ mmol L}^{-1}$ ) containing  $0.1 \text{ mol L}^{-1}$  KCl as supporting electrolyte, (A) on the bare GCE (a), MWCNTs-COOH/GCE (b), bdpY/GCE (c), PW<sub>11</sub>Co/GCE (d), and (bdpy)PW<sub>11</sub>Co/MWCNTs-COOH/GCE (e) at pH 3; Scan rate:  $50 \text{ mV s}^{-1}$ . (B) On the (bdpy)PW<sub>11</sub>Co/MWCNTs-COOH/GCE at different pHs. Inset shows variation of normalized  $i_{pa}$  and  $\Delta E_p$  extracted from cyclic voltammograms of (bdpy)PW<sub>11</sub>Co/MWCNTs-COOH/GCE. Normalized  $i_{pa}$  and  $\Delta E_p$  are  $(i_{pa}(\text{max}) - i_{pa})/i_{pa}(\text{max})$  and  $(\Delta E_p(\text{max}) - \Delta E_p)/\Delta E_p(\text{max})$ , respectively. (C) On the (bdpy)PW<sub>11</sub>Co/MWCNTs-COOH/GCE at different scan rates from  $10$  to  $140 \text{ mV s}^{-1}$ . The inset shows variations of the cathodic peak currents with square root of scan rates